

# A Seismological Study of the Sos Enattos Area—the Sardinia Candidate Site for the Einstein Telescope

Matteo Di Giovanni<sup>\*1,2,3</sup>, Carlo Giunchi<sup>1</sup>, Gilberto Saccorotti<sup>1</sup>, Andrea Berbellini<sup>4</sup>, Lapo Boschi<sup>4,5,6</sup>, Marco Olivieri<sup>4</sup>, Rosario De Rosa<sup>7,8</sup>, Luca Naticchioni<sup>9,10</sup>, Giacomo Oggiano<sup>11,12</sup>, Massimo Carpinelli<sup>11,12</sup>, Domenico D'Urso<sup>11,12</sup>, Stefano Cuccuru<sup>11,12</sup>, Valeria Sipala<sup>11,12</sup>, Enrico Calloni<sup>7,8</sup>, Luciano Di Fiore<sup>7</sup>, Aniello Grado<sup>13</sup>, Carlo Migoni<sup>14</sup>, Alessandro Cardini<sup>14</sup>, Federico Paoletti<sup>15</sup>, Irene Fiori<sup>16</sup>, Jan Harms<sup>2,3</sup>, Ettore Majorana<sup>9,10</sup>, Piero Rapagnani<sup>9,10</sup>, Fulvio Ricci<sup>9,10</sup>, and Michele Punturo<sup>17</sup>

## Abstract

The recent discovery of gravitational waves (GWs) and their potential for cosmic observations prompted the design of the future third-generation GW interferometers, able to extend the observation distance for sources up to the frontier of the Universe. In particular, the European detector Einstein Telescope (ET) has been proposed to reach peak strain sensitivities of about  $3 \times 10^{-25} \text{ Hz}^{-1/2}$  in the 100 Hz frequency region and to extend the detection band down to 1 Hz. In the bandwidth [1,10] Hz, the seismic ambient noise is expected to represent the major perturbation to interferometric measurements, and the site that will host the future detectors must fulfill stringent requirements on seismic disturbances. In this article, we conduct a seismological study at the Italian ET candidate site, the dismissed mine of Sos Enattos in Sardinia. In the range between few mHz to hundreds of mHz, out of the detection bandwidth for ET, the seismic noise is compatible with the new low-noise model (Peterson, 1993); in the [0.1,1] Hz bandwidth, we found that seismic noise is correlated with sea wave height in the northwestern Mediterranean Sea. In the [1,10] Hz frequency band, noise is mainly due to anthropic activities; within the mine tunnels ( $\approx 100$  m underground), its spectrum is compliant with the requirements of the ET design. Noise amplitude decay with depth is consistent with a dominance of Rayleigh waves, as suggested by synthetic seismograms calculated for a realistic velocity structure obtained from the inversion of phase- and group-velocity dispersion data from array recording of a mine blasting. Further investigations are planned for a quantitative assessment of the principal noise sources and their spatiotemporal variations.

**Cite this article as** Di Giovanni, M., C. Giunchi, G. Saccorotti, A. Berbellini, L. Boschi, M. Olivieri, R. De Rosa, L. Naticchioni, G. Oggiano, M. Carpinelli, et al. (2020). A Seismological Study of the Sos Enattos Area—the Sardinia Candidate Site for the Einstein Telescope, *Seismol. Res. Lett.* **XX**, 1–13, doi: [10.1785/0220200186](https://doi.org/10.1785/0220200186).

[Supplemental Material](#)

## Introduction

Modern fundamental physics experiments are often significantly affected by the environment in which they are conducted. For instance, in situ radioactivity or particle background hinders the attempts to measure rare particle interaction or interactions with dark matter (Cahn and Goldhaber, 2009). Likewise, it has been shown that light pollution and atmospheric conditions need to be accounted in the selection criteria for ground-based telescopes (Schroeder, 2000). The surrounding environment also plays a crucial role for gravitational-wave (GW) detectors, because ground motion, sound, and other environmental disturbances can limit the sensitivity of the detector and reduce its duty cycle.

So far, GWs have been observed by means of a network of three second-generation Michelson interferometers, with an arm

1. Istituto Nazionale di Geofisica e Vulcanologia – Sezione di Pisa, Pisa, Italy; 2. Gran Sasso Science Institute, L'Aquila, Italy; 3. Laboratori Nazionali del Gran Sasso, Istituto Nazionale di Fisica Nucleare, Assergi, Italy; 4. Istituto Nazionale di Geofisica e Vulcanologia—Sezione di Bologna, Bologna, Italy; 5. Dipartimento di Geoscienze, Università degli Studi di Padova, Padua, Italy; 6. Institut des Sciences de la Terre de Paris (ISTeP), Sorbonne Université, CNRS, INSU, Paris, France; 7. Dipartimento di Scienze Fisiche, Università degli Studi di Napoli Federico II, Naples, Italy; 8. Istituto Nazionale di Fisica Nucleare—Sezione di Napoli, Naples, Italy; 9. Istituto Nazionale di Fisica Nucleare—Sezione di Roma, Rome, Italy; 10. Dipartimento di Fisica, La Sapienza Università di Roma, Rome, Italy; 11. Dipartimento di Chimica e Farmacia, Università degli Studi di Sassari, Sassari, Italy; 12. Laboratori Nazionali del Sud, Istituto Nazionale di Fisica Nucleare, Catania, Italy; 13. Istituto Nazionale di Astrofisica, Osservatorio Astronomico di Capodimonte, Naples, Italy; 14. Istituto Nazionale di Fisica Nucleare—Sezione di Cagliari, Monserrato, Italy; 15. Istituto Nazionale di Fisica Nucleare—Sezione di Pisa, Pisa, Italy; 16. European Gravitational Observatory, Cascina, Italy; 17. Istituto Nazionale di Fisica Nucleare—Sezione di Perugia, Perugia, Italy

\*Corresponding author: [matteo.digiovanni@gssi.it](mailto:matteo.digiovanni@gssi.it)

© Seismological Society of America

length of the order of the km: advanced Laser Interferometer Gravitational-wave Observatory (LIGO) Hanford and Livingston detectors (LIGO Scientific Collaboration, 2015) in the United States, and Advanced Virgo (Virgo Collaboration, 2015) in Italy. Currently, a Japanese underground interferometer (KAGRA GRAVitational-wave detector [KAGRA], KAGRA Collaboration, 2019) has recently joined the network. These detectors are designed to observe GWs in the frequency band between 10 Hz and a few kHz. In this frequency range, the current generation of GW detectors has already observed astrophysical sources, such as coalescing binary systems of neutron stars and black holes (LIGO Scientific Collaboration and Virgo Collaboration, 2019a). Other astrophysical sources are expected to be detectable in the same frequency range, like supernovae (Evans and Zanolin, 2017) and isolated neutron stars (LIGO Scientific Collaboration and Virgo Collaboration, 2019b). GW detectors measure the fractional variation  $\delta L/L$  (strain) of the distance between the mirrors and the beam splitter due to an incoming GW. Today, GW interferometers can achieve a strain sensitivity less than  $2 \times 10^{-23} \text{ Hz}^{-1/2}$  around 100 Hz. Because ground motion induced by seismic noise is order of magnitude larger than the typical measured strain, and it is the main source for duty cycle interruption of GW detectors (Effler *et al.*, 2015), active and passive seismic insulators have been installed in GW detectors, with the test masses (i.e., the mirrors of the interferometers) suspended to a chain of filters. For example, in the Virgo detector seismic noise is attenuated by a cascade pendulum in which each element has nearly equal frequency  $\nu_0$ . This way, the amplitude of vibrations of frequency  $\nu$  is reduced by a factor  $(\nu/\nu_0)^{-2}$  at each stage of the pendulum. This system is also known as superattenuator (Virgo Collaboration, 2011). Yet, below 20 Hz, the detection capability of GWs might still be reduced by seismic disturbances, depending on their magnitude.

Seismic noise is generated by oceanic microseisms and, at frequencies  $f > 1$  Hz, by anthropic activities (e.g., Piccinini *et al.*, 2020; Poli *et al.*, 2020; for the effect on GW detectors, see Virgo Collaboration, 2004, 2006; Saccorotti *et al.*, 2011). GW data may be affected by seismic waves in multiple ways, including light in the output laser beams scattered by seismically excited surfaces (e.g., elements on optical benches) and coupled back into the main beam of the interferometer (Virgo Collaboration, 2010), unwanted motions of the suspended mirrors caused by residual noise passing through the seismic isolation system, coupling of the residual tilt of the suspended elements (i.e., filters and test masses, Virgo Collaboration, 2011). Moreover, mass density fluctuations can interact directly with the mirrors through gravitational forces. This is also referred to as Newtonian noise (NN) or gravity gradient noise (Saulson, 1984; Harms, 2019).

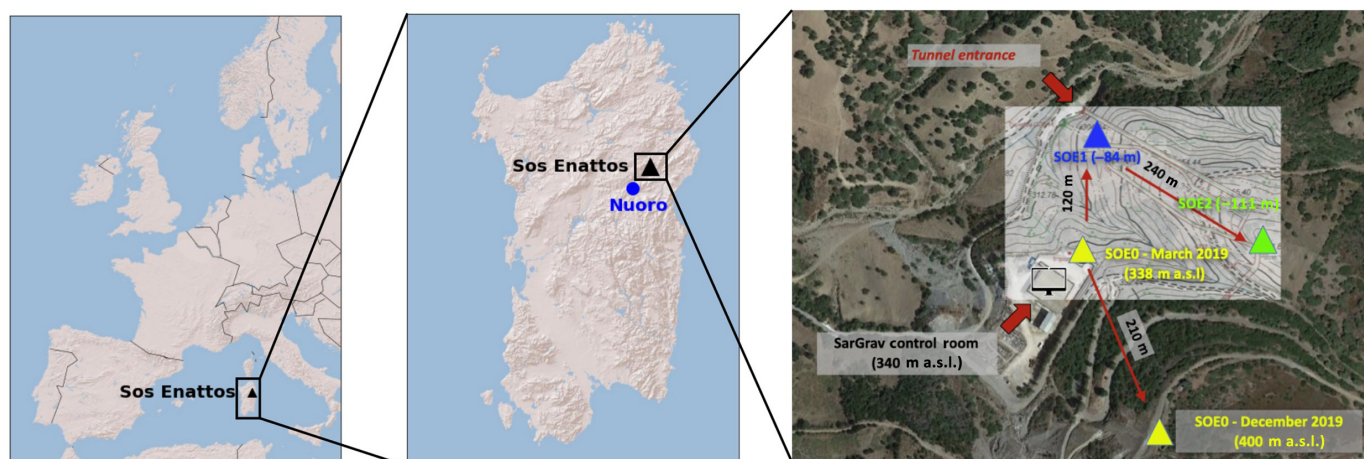
To extend the detector bandwidth to frequencies as low as  $\approx 1$  Hz, the GW community has been planning a major technological leap since 2010 (Einstein Telescope [ET] Science Team, 2010), 5 yr before the first observing run of

Advanced LIGO even began, starting to design a third-generation GW observatory named ET (ET Science Team, 2010, 2011; Amann *et al.*, 2020). The plan is to host the detector in an underground tunnel system at depths between 200 and 300 m (with optimal depth to be determined depending on the noise level and other characteristics of the site), to mitigate seismic motion at the input of the suspension system. The detector will have the shape of an equilateral triangle, with 10 km long sides, each hosting three pairs of nested interferometers observing in parallel (xylophone configuration; Hild *et al.*, 2009). This configuration yields a higher wideband sensitivity with respect to current generation (ET Science Team, 2010, 2011). Collocating multiple interferometers in the same observatory also results in more stringent constraints on the seismicity rate but simplifies the measurement of GW polarization, which requires a minimum of two detectors. Moreover, the ET detector bandwidth starting at  $f \approx 1$  Hz will provide longer observing time windows for compact object binary mergers. In the [1,10] Hz band, ET design sensitivity is expected to be affected by seismic noise sources of both natural and anthropogenic origin. Therefore, geodynamical stability and low noise induced by human activities are of paramount relevance for evaluating the candidate sites for the construction of ET (Amann *et al.*, 2020).

The Sos Enattos mine, now dismissed but still manned for environmental safety, was selected as one of the candidate sites to host ET (ET Science Team, 2011). The mine is located in Sardinia, 30 km northeast of the city of Nuoro, and includes a complex network of tunnels (50 km total length). Nowadays, through one of these tunnels, named Rampa Tupeddu, is possible to reach a depth of about 120 m (Fig. 1). In the European context, Sardinia is known for its very low seismic hazard (Stucchi *et al.*, 2004, 2011; Woessner *et al.*, 2015) and low population density (Eurostat, 2019). The seismic and environmental studies at Sos Enattos started in 2010, but, only in 2014, the first long-term observations were undertaken (Naticchioni *et al.*, 2014). Since 2018, the mine hosts SARDinia-GRAVity (Naticchioni, 2018), a laboratory for fundamental physics research in low-ambient-noise environments that also provides a research and development infrastructure for ET. In the following, we recap the general features of the Sos Enattos site and present the first results from an ongoing, long-term observational survey, which started in March 2019, aimed at characterizing seismic noise at Sos Enattos and its variations with depth.

## Sos Enattos: A Low-Seismicity and Low-Noise Site

As opposed to continental Italy and most of the Mediterranean basin, Sardinia has long been known to be seismically quiet, which is an essential feature for a site hosting a third-generation GW detector like ET, to prevent frequent duty cycle interruption. The Italian Seismological Instrumental and Parametric Database (ISIDe) catalog (ISIDe Working



Group, 2007) reports only 51 earthquakes (all with magnitude less than 4.7) between 1980 and 2020, within 170 km from Sos Enattos. Of these events, only 10 were recorded at less than 50 km from Sos Enattos, all with  $M_L \leq 2.5$ . The relatively larger magnitude (i.e.,  $M > 3$ ) ones occur offshore under the Tyrrhenian sea. Very sparse seismicity in that area is also reported by the CPTI15 historical earthquake catalog covering the years from 1000 to 2014 (Rovida *et al.*, 2019), with only one inland ( $M = 4.9$  near Cagliari, 1616) and two offshore events ( $M = 4.8$  and  $5.4$  in 1970 and 1977, respectively). Accordingly, the seismic hazard map of Italy attributes to Sardinia, an upper-bound peak ground acceleration (PGA) of  $0.05g$  with a 10% probability of exceedance in 50 yr (Stucchi *et al.*, 2004, 2011). This is one of the lowest reported estimates of PGA throughout the Euro-Mediterranean area (Woessner *et al.*, 2015).

These observations are in agreement with the geodynamic evolution of the Corsica–Sardinia microblock (e.g., Carmignani *et al.*, 2004; Faccenna *et al.*, 2014; Magrini *et al.*, 2020), which, after completing the clockwise rotation due to the opening of the Liguro-Provençal basin roughly between 30 and 15 Ma, remained unaffected by the fast extension, leading to the formation of the Tyrrhenian Sea in the last 15 Ma. This is also confirmed by the present-day deformation, showing very little motion of the Corsica–Sardinia microblock with respect to Eurasia plate (Faccenna *et al.*, 2014). In particular, the mine site lays on a crystalline basement of mica schist, quartzite, orthogneiss, and granitoid rocks, that is known to provide a stable environment for the construction of large underground facilities (Beker *et al.*, 2011). Because these rocks are characterized by a low porosity, there are no significant groundwater masses in the area, as confirmed by electrical resistivity tomography (Naticchioni *et al.*, 2020).

The area around Sos Enattos is scarcely inhabited. According to Eurostat (2019), the average population density of Sardinia is low ( $70/\text{km}^2$ ) and drops to  $13/\text{km}^2$  within 10 km from the site. There are no major railways, highways, large industrial, or agricultural plants in a range of tens of kilometers

**Figure 1.** (Left) Location of Sos Enattos in Europe. (Center) Location of Sos Enattos in Sardinia. (Right) Placement of the seismic stations at the mine. m a.s.l., meter above sea level. The color version of this figure is available only in the electronic edition.

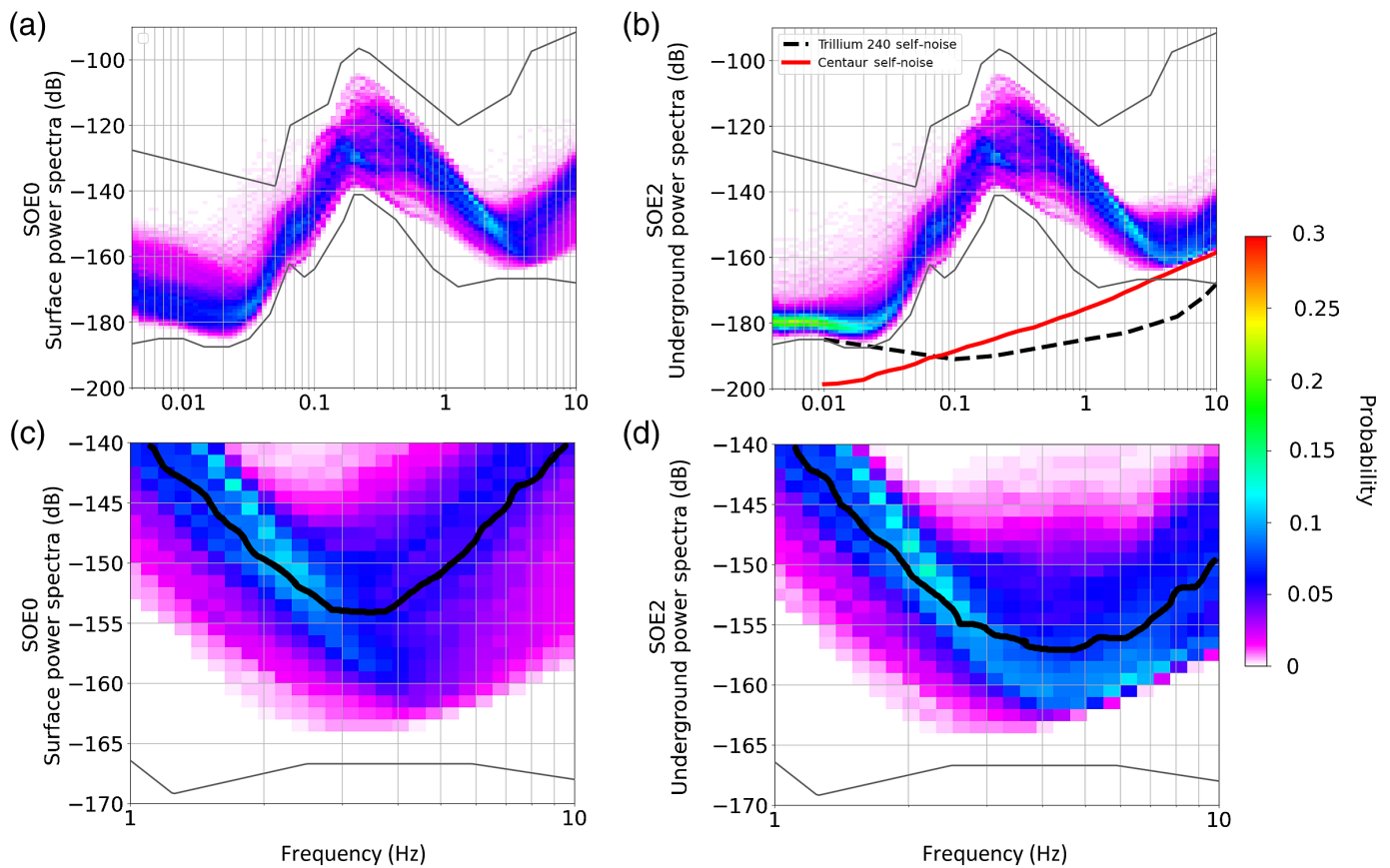
from the site. It is likely that anthropic noise at Sos Enattos is limited to very local activities, which, to our knowledge, only include mine maintenance (vehicles driving at the site, lorries unloading their cargo, active water pumps, miners inspecting the site) and, possibly, farming activities in the nearby fields and pastures. All these activities can be controlled and would be interrupted when ET will become operational.

## Site Characterization

### Instruments and noise environment

At the onset of the measurement campaign (end of March 2019), three seismic stations were installed in Sos Enattos (Table 1; Fig. 1): a Güralp 3ESPCD (Güralp, 2020) on the surface (station SOE0, 338 m above sea level) and two Nanometrics Trillium 240 (Nanometrics, 2005) at a depth of 84 m (SOE1) and 111 m (SOE2) with respect to SOE0. In December 2019, SOE0 was moved in a dedicated vault 210 m southeast (400 m above sea level, Fig. 1). This was also the occasion to replace the sensor, malfunctioning below 0.1 Hz, with a Trillium 240. Accordingly, only the spectra from 2020 are shown in this section. At the time of the installation, either SOE0 or SOE2 was supposed to be included into the Italian seismic network, managed by the Istituto Nazionale di Geofisica e Vulcanologia (INGV). Both stations were thus set to operate without pre-amplification, as required for earthquake monitoring.

The probabilistic power spectral density (PPSD) of the vertical channels of SOE0 (Fig. 2a) and SOE2 (Fig. 2b) is obtained using the method of McNamara and Buland (2004), over the 1 January 2020 to 30 April 2020 time span. As the power spectral densities (PSDs) of SOE1 and SOE2 are very similar in the frequency band up to 10 Hz (Fig. 3a), we disregard SOE1 and only



compare recordings at SOE0 and SOE2. Between  $5 \times 10^{-3}$  Hz and  $2 \times 10^{-1}$  Hz, the PPSD of SOE2 follows the new low-noise model (NLNM; Peterson, 1993). Between 0.1 and 1 Hz, the PPSD exhibits peaks related to microseisms. In particular, the peak at  $f \simeq 0.2$  Hz is caused by secondary microseisms, also called double-frequency microseism (DFM) occurring at twice the frequency of ocean waves and originating from nonlinear interactions of standing ocean waves causing a pressure wave propagating toward the ocean floor (Hillers *et al.*, 2012; Amann *et al.*, 2020). The other peak, barely visible at  $f \simeq 0.06$  Hz, is associated with primary microseisms that originate from wave motion in shallow waters (Longuet-Higgins, 1950; Chevrot *et al.*, 2007; Hillers *et al.*, 2012).

**Figure 2.** Probabilistic power spectral densities (PPSDs) of the vertical channels for (a) SOE0 and (b) SOE2 during 2020. The frequency ranges from 0.02 Hz (240 s) to 50 Hz (0.02 s). The new low-noise model (NLNM), new high-noise model (NHNM), and detector noise curves are also shown. (c,d) Zoom of (a,b) in the [1,10] Hz band including the median of the PPSD (black line). The color version of this figure is available only in the electronic edition.

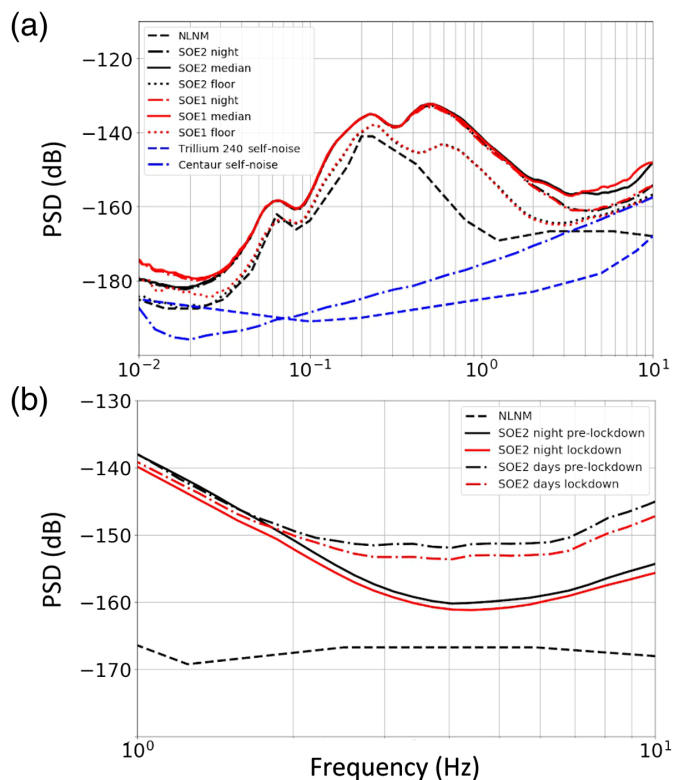
In the frequency interval [1,10] Hz, the median of the PPSD of SOE0 shows a wide minimum around 3.5 Hz at  $\simeq -154$  dB, then linearly increasing up to  $\simeq -140$  dB at 10 Hz (Fig. 2c). In the same frequency interval, the PPSD of SOE2 shows a

TABLE 1  
**Seismic Stations**

Station	Latitude (°)	Longitude (°)	Altitude m a.s.l.	Depth (m)	Sensor	Digitizer
SOE0 (2019)	40.444298	9.456815	338	–	Güralp 3ESPCD 120 s	Embedded
SOE0 (2020)	40.442520	9.457812	400	–	Nanometrics Trillium 240 s	Nanometrics Taurus
SOE1	40.445509	9.456854	254	–84	Nanometrics Trillium 240 s	Nanometrics Taurus
SOE2	40.445457	9.456988	227	–111	Nanometrics Trillium 240 s	Nanometrics Centaur

The depth of SOE1 and SOE2 is determined with respect to a standard reference point on top of the mine. m a.s.l., meter above sea level.





**Figure 3.** (a) Comparison between SOE1 and SOE2. Solid lines show the median of the PPSDs. Dotted-dashed lines refer to night only. Dotted lines represent the minimum of the PPSD. Peterson's NLNM is also shown. (b) Median by day and at night of the PPSD of SOE2 before and after the 2020 COVID lockdown in Italy. The medians are computed during the three weeks before and the first three weeks after the onset of the lockdown (11 March). PSD, power spectral density. The color version of this figure is available only in the electronic edition.

minimum around 4.5 Hz at  $\approx -157$  dB and increasing to  $\approx -150$  dB at 10 Hz (Fig. 2c). The values of SOE0 and SOE2 meet the criteria of ET that require a noise level of  $-154$  dB at 4 Hz (ET Science Team, 2010, 2011). However, it must also be considered that PSD estimates at frequencies above 4 Hz meet the noise floor of the digitizer shown in Figure 2b, so the actual noise level could be even lower.

As a first attempt to evaluate the anthropic contribution to the recorded noise, we compare the overall and nighttime PPSDs. At both underground stations, the two estimates are distinct only at frequencies above 2 Hz, in which they attain a maximum difference of about 5 dB (i.e., a factor of 1.8 in amplitude; Fig. 3a). Similar results are obtained by comparing the PPSDs taken before and after the establishment of containment measures of the COVID-19 pandemic ("lockdown"), when severe restrictions on vehicle traffic and interruption of all nonessential human activities were imposed. Again, the pre- and post-lockdown PPSD estimates are distinguishable only above 2 Hz, in which they differ by about 2 dB (i.e., less than

a factor of 1.25 in amplitude; Fig. 3b). Such decreases are comparable with what is reported by Poli *et al.* (2020) and Piccinini *et al.* (2020), who observed post-lockdown power drops on the order of 50% at several sites in continental Italy. These two examples helped to discriminate better the spectral signature of cultural (anthropic) noise sources and to quantify their contribution to the overall noise power. In conclusion, the effects of anthropic activities on underground seismic noise at Sos Enattos, albeit present, are small. We find that the noise power meets the ET requirement of  $-154$  dB at 4 Hz and, to the best of the data currently available, it is reasonable to consider Sos Enattos among the 10% quietest sites in the world, at least for the [4,7] Hz frequency band (Fig. 4). This represents a conservative estimate, in light of the aforementioned resolving limitations associated with the digitizer noise (Figs. 2b and 3a). A final point concerns the discrimination of all those local noise sources that will be eliminated by the time ET will be functioning (i.e., maintenance operations at and around the mine, or other small-scale human activities in the neighborhood). To answer this question, specific surveys are in progress for monitoring seismic noise using dense seismometer arrays, which, through wavefield decomposition, will permit to assess quantitatively location and strength of the principal noise sources.

### Seismic velocities

Constraints on the ground velocity profiles at the site are obtained from the analysis of ground motion associated with the drilling-and-blasting enlargement of a gallery of the mine. The blasting was conducted on 18 October 2018, and it consisted of five consecutive explosions fired at 0.25 s intervals, at a depth of about 150 m beneath the surface. We recorded the signals generated by the blasts using a linear array of five seismometers positioned at distances in between  $\approx 450$  and 2000 m from the surface projection of the shot point (Table 2). By fitting the first-arrival times with a straight line, we obtain an apparent *P*-wave velocity of  $V_p = 4.80 \pm 0.13$  km/s (Fig. 5a).

We then use a frequency–time analysis of recorded data to estimate the Rayleigh-wave group velocity. First, we calculate the envelopes of the signals at individual stations, using a Gaussian filter with parameter  $\alpha = 10$  (Levshin *et al.*, 1972), spanning 25 center frequencies within the [3,8] Hz frequency interval. For each frequency, we use the time differences between the maxima of the envelopes at the different stations to derive group-velocity estimates for each independent station pair. For each frequency bin, we then average those velocity estimates, thus obtaining the dispersion relationship of Figure 5. Subsequently, we use a *p*– $\omega$  stack procedure (e.g., Herrmann, 2013), to derive a phase-velocity dispersion curve over the [2,5.5] Hz frequency range (Fig. 5c).

Under the assumption that both the group- and phase-velocity dispersions are associated with the fundamental mode of Rayleigh waves, we perform a joint inversion of those curves

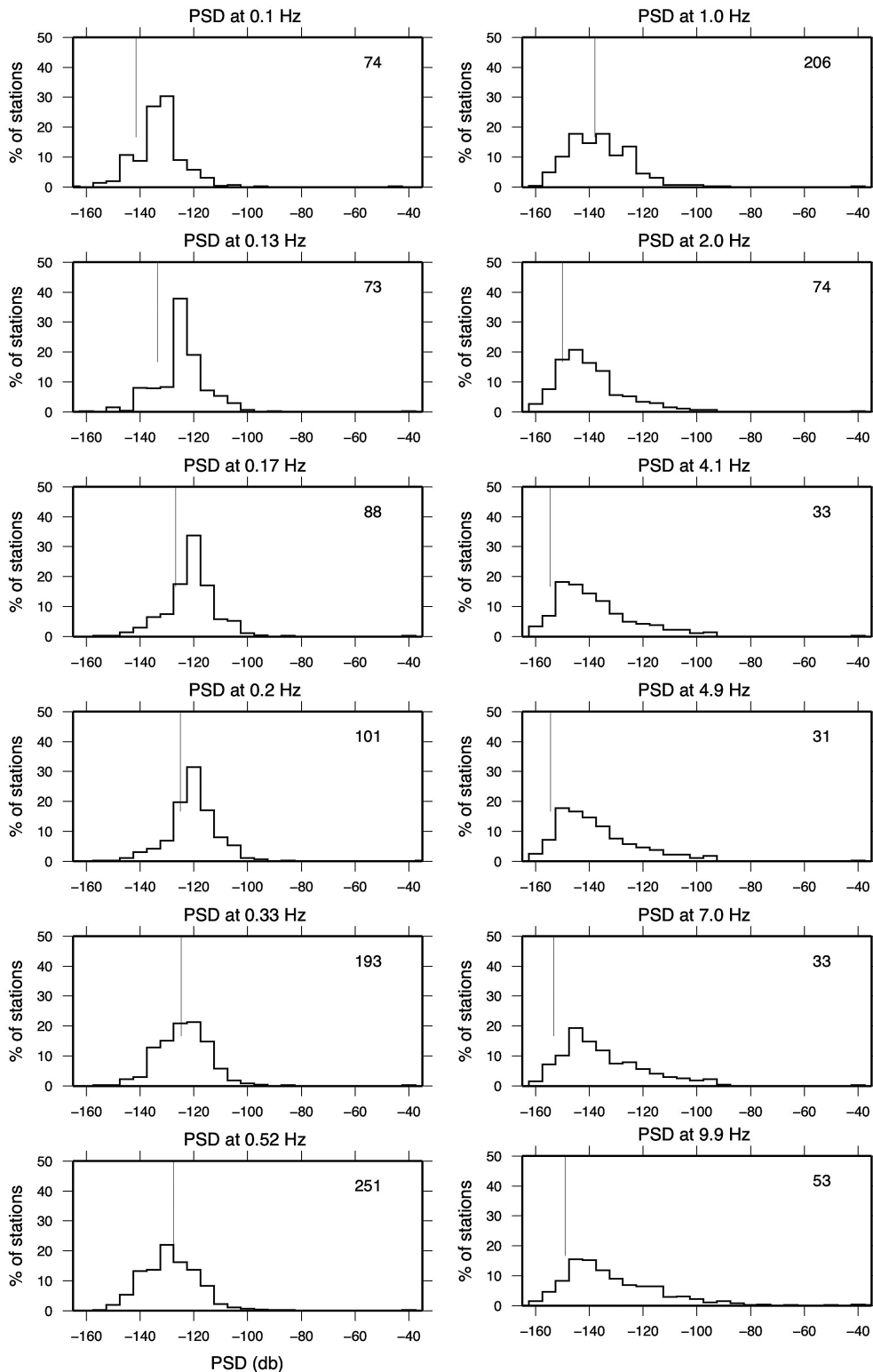


**Figure 4.** Evaluation of the noise level for SOE2 at global scale. For each frequency bin, on top of each frame, we calculate the mean PSD (in dB) for each of the 445 stations that compose the Incorporated Research Institutions for Seismology virtual network `_FDSN+ALL` in the period of 1 January 2020 to 30 April 2020. In each frame, the vertical bar indicates the average level of noise as observed at SOE2 in the same time span (Fig. 2b), whereas the number on the top right corner indicates the SOE2 ranking with respect to the selected global network.

for a shear-wave velocity ( $V_S$ ) ground profile. We conduct the inversion using the GEOPSY code (Wathelet *et al.*, 2020). We used a simple parameterization of the subspace, consisting of two, 100-meter-thick layers overlying a half-space. Density is kept constant at  $2600 \text{ kg/m}^3$ , whereas the Poisson ratio is let to vary in the 0.2–0.3 range. At the end of the inversion, we consider as acceptable those velocity profiles for which corresponding dispersion curves are included in the  $\pm 0.5$  sigma interval around the experimental dispersions (Fig. 5b,c). Shear-wave velocities span the  $[1.8, 2.0]$ ,  $[2.0, 2.2]$ , and  $[2.5, 2.7]$  km/s intervals for the two layers and the half-space, respectively. The corresponding  $P$ -wave velocities, respectively, span the  $[3.1, 3.6]$ ,  $[3.4, 0.0]$ , and  $[3.4, 0.0]$  intervals. The retrieved model suggests a substantial homogeneity of the shallow velocity structure, in agreement with the lack of amplification effects discussed in the next section.

### Seismic noise amplitude ratio

To better quantify the variation of noise amplitude with depth, Figure 6 shows the 5th, 50th, and 95th percentiles of the ratios of the amplitude spectral density for the vertical channels of the surface (SOE0) and underground (SOE2) seismometers. We do not extend such comparison to station SOE1, given the similarity of its spectra with those derived at SOE2 (Fig. 3a). At the underground site, amplitude decay starts to be significant at frequencies above 2 Hz, till reaching a factor of 5 at 10 Hz. For interpreting these data, we use a modal

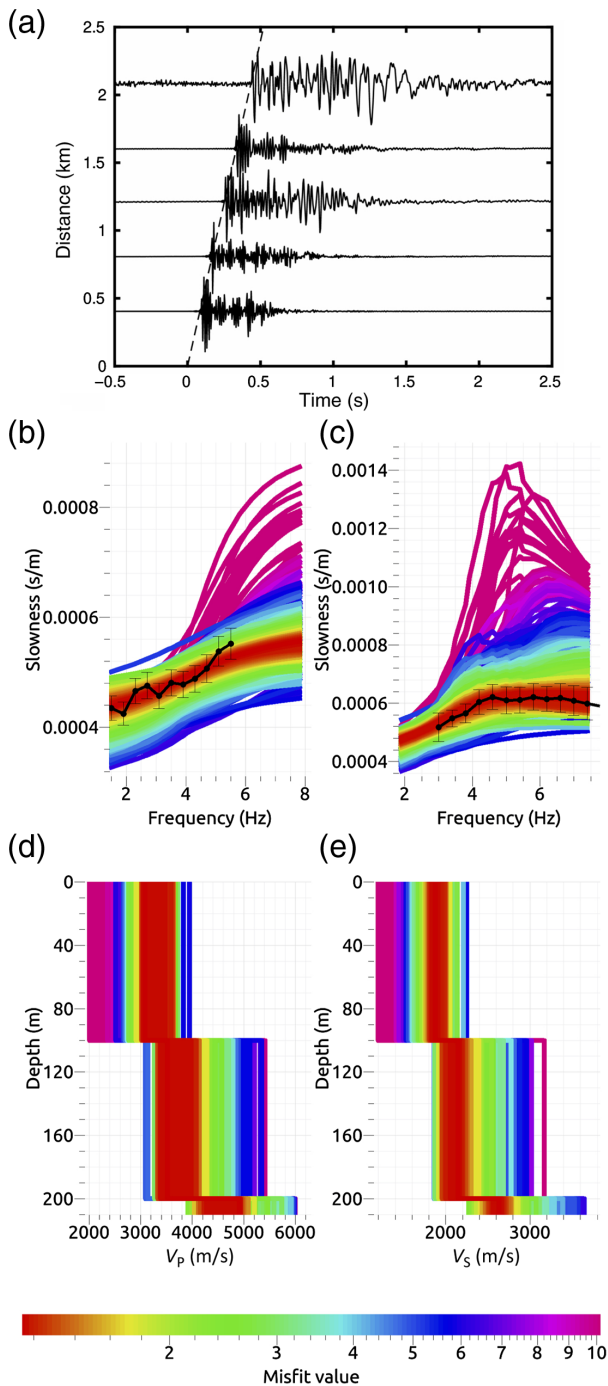


**Figure 5.** (a) Recordings of the vertical component of ground velocity associated with the blasting fired at 8:36:10 UTC on 18 October 2018. Traces are individually normalized to their maximum amplitude. The dashed line marks the 4.8 km/s dromochrone. (b) Phase velocities measured over the [2,5.5] Hz frequency interval (black dotted line), compared with the predictions from the ensemble of investigated velocity models (colored patches). (c) The same as in (b), but for group-velocity data measured over the [3,8] Hz frequency range. (d) Compressional- and (e) shear-wave velocity models derived from inversion of the phase- and group-velocity dispersions shown in (b,c). Colors in (b–e) correspond to the inversion misfit, according to the color bar at the bottom. The color version of this figure is available only in the electronic edition.

summation approach (Herrmann, 2013) and compute synthetic Rayleigh-wave seismograms from an arbitrary, vertical point source located at 10 km distance and recorded at a receiving station at the surface (as for SOE0) and at 111 m depth (as for SOE2). The seismic model used in the simulation is obtained by extending the half-space of the velocity profiles of Figure 5 down to a depth of 2 km, where the crustal velocity model of Magrini *et al.* (2020) is then adopted. From the resulting synthetic seismograms, we finally obtain the expected amplitude spectral ratio between the surface and underground sensors. As it is shown in Figure 6, the simulated Rayleigh-wave amplitude ratios are in good agreement with the observed ones. The main discrepancies are noted at frequencies below 0.03 Hz and above 4 Hz. Over those particular frequency band, the observed spectral ratios are likely conditioned by the sensor and digitizer self-noise, respectively. In conclusion, the amplitude decay with depth becomes significant at frequencies above  $\approx 2$  Hz, consistently with what is expected for Rayleigh-wave propagation in the previously derived velocity model.

### Horizontal-to-vertical spectral ratios

Further hints on the elastic properties of the subsurface are gained through analysis of the horizontal-to-vertical spectral ratios (HVSRs) of seismic noise (Nakamura, 1989, 2008). Although the theoretical meaning of HVSR is still under debate (Lunedei and Malischewsky, 2015), it is now widely accepted that peaks in the HVSR function correspond to the S-wave resonance frequencies, when a marked impedance contrast exists between shallow, soft layers and an underlying bedrock. Consequently, the HVSR constitutes a cost-effective and rapid tool for evaluating both site amplification effects and constraining the elastic properties of the shallowest geological layers.

To estimate the HVSR at Sos Enattos, we use four months of continuous recording from SOE0 and follow the procedure of Atakan *et al.* (2004). After calculating the fast Fourier transform over 1-hour-long segments, the spectra are smoothed using a Konno–Ohmachi function (Konno and Ohmachi, 1998), and the two horizontal components (N, E) are composed through their geometric mean, that is,  $H = \sqrt{H_N \times H_E}$ . The average of the hourly HVSRs is shown in Figure 7, alongside with the corresponding 5th and 95th percentiles intervals. In the [0.2,10] Hz frequency interval, the HVSR curve does not exhibit any peak, and has a constant value of 1. For a shallow, soft layer of thickness  $h$  overlaying a bedrock, the S-wave resonance frequency  $f_c$  is given by  $f_c = \frac{V_s}{4h}$  (Parolai *et al.*, 2002), in which  $V_s$  is the shear-wave velocity of the layer. We may use this equation to constrain the minimum depth for which no significant impedance contrasts exist. By considering  $V_s$  in the [2.0, 2.7] km/s range (Fig. 5), and the lower frequency bound of the flat portion of the HVSR curve (0.2 Hz), we infer that there are no significant impedance contrasts down to depths of about [2500, 3000] m below the

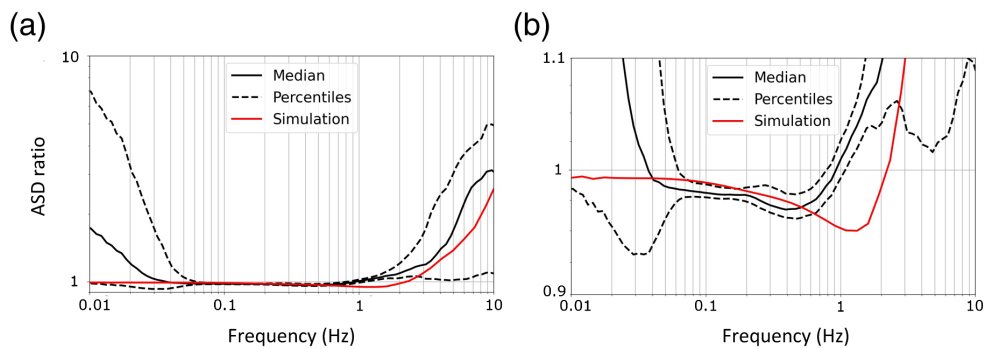


**Figure 6.** (a) Vertical component SOE0/SOE2 amplitude spectral density (ASD) ratio (black line) and 5th and 95th percentiles (dashed lines) compared with the corresponding amplitude ratios estimated from synthetic seismograms (red line). (b) Zoom of (a) around ASD ratio = 1. The color version of this figure is available only in the electronic edition.

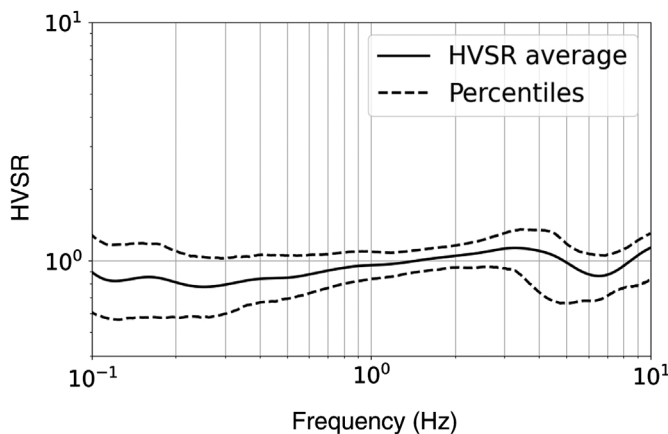


**Figure 7.** Average horizontal-to-vertical spectral ratio (HVSr) of SOE0 in the period of 1 January 2020 to 30 April 2020. Dashed lines are the 5th and 95th percentiles.

surface. This is not surprising, in light of the previously summarized geological features of the site.

## Correlation Studies Earthquake detection

To further investigate the data, seismic waveforms from SOE0, SOE1, and SOE2 are also correlated in search for earthquakes, in particular, low-magnitude local events that could have been missed. Earthquake signal enhances the correlation between different stations that, from the source perspective,

are at same azimuth and distance. Continuous data are correlated by filtering 10 min long segments in the [1,10] Hz band to prevent microseismic noise from actually blinding the analysis. Both vertical and horizontal channels are used, and because, in the frequency band of interest, SOE0 did not experience any issue, the analysis is extended also on the 2019 data. In total, 31 teleseismic events are found using this method from 1 April 2019 to 31 August 2019 and 38 more from 1 January 2020 to 30 April 2020. Besides these arrivals, two extra peaks emerge at epochs in which no events are reported in the INGV catalog (ISIDE Working Group, 2007). For these two events, *P*-*S* travel-time difference suggests a local origin. Data from SOE0 are integrated with those from nearby permanent seismic stations (IV.DGI, IV.AGL, MN.VSL; Boschi *et al.*, 1991; ISIDE Working Group, 2007), and localization is performed using NonLinLoc (Lomax *et al.*, 2009). Table 3 shows the results of the inversion, together with an estimate of the local magnitude. However, these localizations, due to the low magnitude, low station count, and the large azimuthal gap, are poorly constrained.

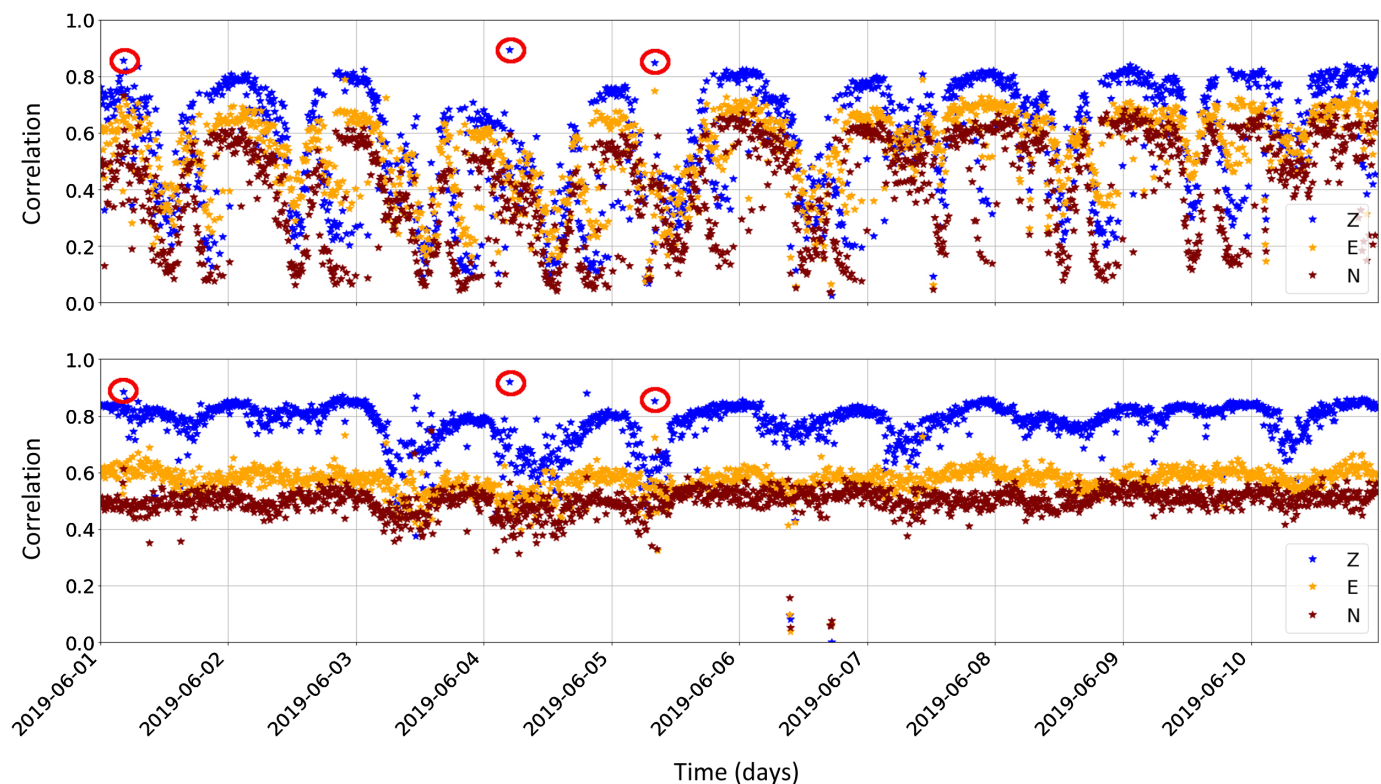
Figure 8 shows sample correlation estimates for the time interval 1 June 2019 to 9 June 2019. We choose to show this

TABLE 2  
**Blast Recording Stations**

Station	Latitude (°)	Longitude (°)	Altitude m a.s.l.	Distance (m)	Sensor	Digitizer
Blast	40.443000	9.457516	228	—	—	—
ST01	40.446552	9.457308	321	405.94	Lennartz 1 s	Nanometrics Centaur
ST02	40.450181	9.458474	336	811.54	Lennartz 1 s	Lunitek Atlas
ST03	40.453792	9.456564	414	1215.58	Lunitek Tellus 1 s	Lunitek Atlas
ST04	40.457348	9.456470	399	1604.57	Lunitek Tellus 1 s	Lunitek Atlas
ST05	40.461423	9.455933	509	2068.96	Lunitek Tellus 1 s	Lunitek Atlas

m a.s.l., meter above sea level.





particular time span as an example of the correlation results, because it includes three events of different nature. In fact, the first two peaks in the correlation values (highlighted by red circles) are associated with the events of 1 June 2019 at 04:26:19 (UTC) from Greek–Albanian border and 4 June 2019 at 04:39:17 (UTC) from Japan (sea). The third peak is the local event  $M_L = 1.8$  on 5 June 2019. Also, correlation between surface and underground stations highlights the night–day cycle showing how local daily surface activities have a limited effect on underground seismic noise. On the other hand, correlation between the underground sensors (bottom panel) oscillates around a constant value and shows only a mild night–day cycle on the vertical component (green points). The vertical channel shows, on average, a correlation of 1.3 times higher than the E and N channels. Applying the same procedure to continuous data recorded in 2020, we find that correlation shows the same main features.

### Sea waves correlation

We study the correlation between seismic data and the sea climate (Hillers *et al.*, 2012), to characterize seismic noise at the site.

**Figure 8.** Correlation between the seismic stations versus time for nine days (1 June 2019 to 9 June 2019) in the 1 Hz <  $f$  < 10 Hz band for all three channels (east–west, blue; north–south, orange; vertical, green). (Top) The night–day cycle is evident when correlating SOE0 and SOE2. (Bottom) The two seismometers underground only show a mild night–day cycle on the vertical channel only. Red circles identify three earthquake detections. The color version of this figure is available only in the electronic edition.

A comprehensive discussion on the generating mechanism of microseisms will not be covered here but can be found in Arduin *et al.* (2011, 2019). For the specific case of Sos Enattos, Naticchioni *et al.* (2014) already discussed the correlation of wind speed and atmospheric pressure variations with seismic noise and conducted a preliminary analysis of correlation between sea wave height and seismic noise. These latter results were obtained, however, from a limited data set consisting of wave height models, calculated at only four points offshore the east coast of Sardinia. Here, we consider a wide region of the Mediterranean Sea taking advantage of the data provided

TABLE 3  
**Local Earthquake Localization**

Time (yyyy/mm/dd hh:mm:ss)	Longitude (°)	Latitude (°)	Depth (km)	$M_L$
2019/06/05 08:05:14	$9.68 \pm 0.01$	$40.565 \pm 0.006$	$17.5 \pm 1.0$	1.8
2019/08/07 22:44:58	$10.7 \pm 0.6$	$40.6 \pm 0.3$	$27.6 \pm 7.8$	1.2

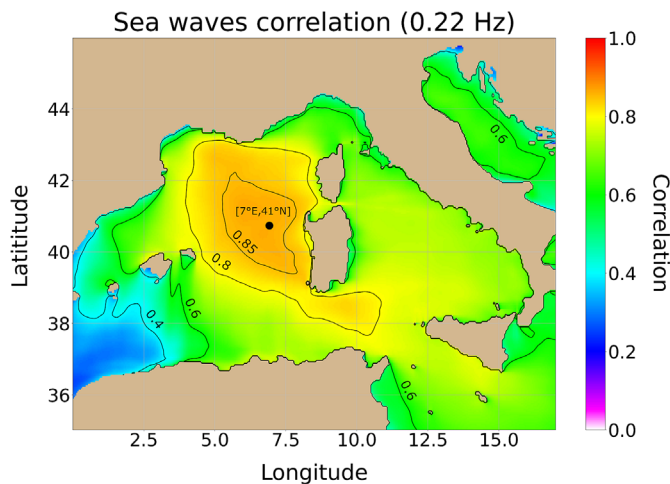


**Figure 9.** Correlation between the average sea wave height and seismic noise at Sos Enattos corresponding to the PSD period that maximizes the correlation. The area of maximum correlation west of Sardinia and Corsica is in agreement with the sources shown in figure 10 of [Chevrot et al. \(2007\)](#). The black dot identifies the point in the grid at which the time series of Figure 10 was extracted. The color version of this figure is available only in the electronic edition.

by the Copernicus Marine Environment Monitoring Service (CMEMS). CMEMS provides reference information on the dynamics of the ocean and marine ecosystems for the global ocean and the European regional seas. In our specific case, we use data from the Mediterranean Sea Waves forecasting system (MEDSEA) ([Korres et al., 2019](#)) and select a subregion of the Tyrrhenian Sea from 1° to 16.5° E and from 35° to 46° N. The MEDSEA data set consists of time series of wave height data sampled every hour (hourly mean) with a coordinates-grid resolution of 4.6 km ([Korres et al., 2019](#)). To achieve this sampling

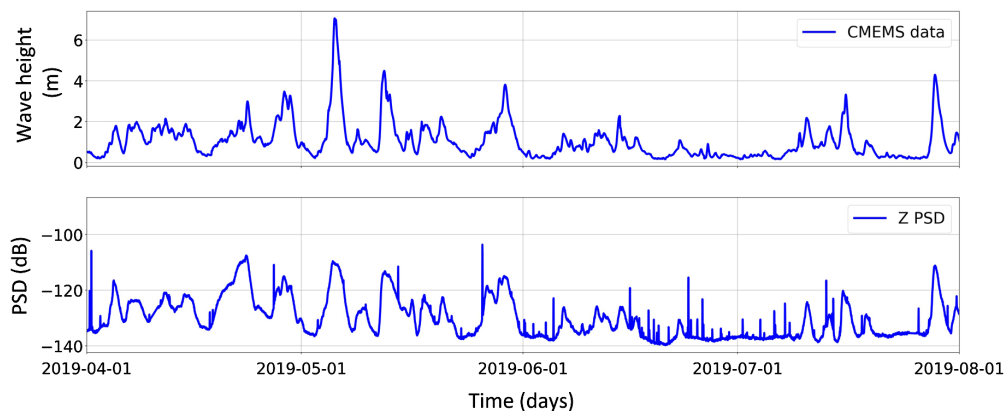


**Figure 10.** (Top) Time evolution of wave height (Copernicus Marine Environment Monitoring Service [CMEMS] data) extracted at the point in the grid identified by the black dot in Figure 9. (Bottom) Comparison of the microseism noise with period equal to 4.5 s, as measured underground at Sos Enattos in 2019, with time evolution of sea wave height in the area of maximum correlation. The color version of this figure is available only in the electronic edition.

and resolution, MEDSEA uses a model that interpolates all available satellite wave height observations ([Korres et al., 2019](#)). For the correlation analysis, we extract the time series of noise power for each period bin of the original PPSD estimates. The time series corresponding to each period of ground oscillation is then cross-correlated against the time series of wave height at the nodes of the MEDSEA model. We find that the average correlation at the nodes in the considered region is maximized for ground vibrations at  $T = 4.5$  s ( $f = 0.22$  Hz), Fig. 9). This result is in agreement with Figure 2, which shows the characteristic microseismic peak at  $f \approx 0.2$  Hz. For this particular period, the areal distribution of the correlation estimates permits to identify a main DFM source in the northwestern Mediterranean Sea (Gulf of Lion), in agreement with the previous findings by [Chevrot et al. \(2007\)](#). In Figure 10, we compare the microseism noise with period equal to 4.5 s, as measured underground at Sos Enattos in 2019, with time evolution of sea wave height in the area of maximum correlation.

## Conclusions and Future Perspectives

In this study, we conducted a seismological investigation at the Sos Enattos former mine (Sardinia, Italy), which is one of the proposed sites to host the next generation of GW detector ET. As expected from its geological and environmental settings, the site is very quiet, and for several frequency bands (e.g.,  $f < 0.5$  Hz,  $2 \text{ Hz} < f < 5 \text{ Hz}$ ) the noise power does not differ significantly from the Peterson's NLNM. In the microseismic band (i.e.,  $0.1 \text{ Hz} < f < 1 \text{ Hz}$ ), the noise spectra exhibit the secondary microseismic peak at frequency around 0.2 Hz. By correlating the temporal evolution of this spectral component with the satellite-based wave height data, we identified the main microseismic source in the west-northwest sector of the Mediterranean Sea, in agreement with the earlier results by [Chevrot et al. \(2007\)](#). In the frequency band of interest for

GW detectors ( $f > 1 \text{ Hz}$ ), Sos Enattos fulfills the ET requirement of  $-154 \text{ dB}$  at 4 Hz and, around that particular frequency, it can be considered among the quietest sites of the Earth. At the underground sites, PSD estimates over the [5–10] Hz frequency interval hit the self-noise floor of the digitizer. As of July 2020, we thus replaced station SOE1 with a high-gain digitizer. Analysis of noise power variations associated with the day-night cycle and with the establishment of the COVID-19 containment measures permitted a first assessment about the

contribution of anthropic activities to the overall noise spectra. To this respect, however, the full characterization of the noise environment at the site requires discriminating individual sources, in turn, quantifying their relative power. Our spectral estimates are likely dominated by the action of very local sources (e.g., the mine maintenance activities), which will be suspended by the time ET will be in operation.

The results presented in this study have important implications for the overall design of an underground GW detector infrastructure. The main outcome, given the general quietness of the site and the geological homogeneity of the subsurface, suggests a configuration of ET requiring only the three vertices of the triangle to be located underground; the potential advantages of this configuration, both practical and economical, deserve an attentive study in which all the implications are evaluated. A full characterization of the noise environment at Sos Enattos implies further measurements to assess the variability of the noise power over much larger spatial and longer temporal scales. In addition, the proper modeling of the NN contribution to the overall noise needs an improved assessment of the composition of the seismic noise wavefield over the whole frequency range of interest with a dedicated measurement campaign. Because of these motivations, new surveys are currently being planned, including seismic noise measurement in boreholes at 200–250 m depths, the deployment of small aperture, dense seismometers arrays aimed at the identification of the principal noise sources in the [1,10] Hz frequency band, and the associated dominant wave types. The extensive measurement campaign will boost the design of the new GW underground detector in Sardinia.

## Data and Resources

The measurement campaign in Sos Enattos is still under way in the framework of the characterization of the two sites proposed for Einstein Telescope (ET), and the data, currently archived at the Istituto Nazionale di Geofisica e Vulcanologia (INGV) servers, are available upon request. Nevertheless, the SOE2 station was recently included in the Italian seismological monitoring network ([Istituto Nazionale di Geofisica e Vulcanologia \(INGV\) Seismological Data Centre, 2006](#)) and is reachable through the webservices of the International Federation of Digital Seismograph Networks (FDSN, <http://www.fdsn.org>) implemented by INGV ([http://cnt.rm.ingv.it/webservices/\\_and/\\_software](http://cnt.rm.ingv.it/webservices/_and/_software)) as IV.SENA. This service provides also data for the other seismic stations used in this article: IV.DGI, IV.AGL, and MN.VSL ([Boschi et al., 1991](#)). Data concerning the average wave height of the Mediterranean Sea are available on the Copernicus Marine Environment Monitoring Service (CMEMS) at [copernicus.eu](http://copernicus.eu). All websites were last accessed in May 2020. Power spectral densities for the virtual network \_FDSN+ALL (Fig. 4) have been obtained from the Incorporated Research Institutions for Seismology (IRIS) webservice Modular Utility for STatistical kNoledge Gathering (MUSTANG, [Casey et al., 2018](#)). Data management, analysis, and visualization have been carried out in Python using ObsPy ([Beyreuther et al., 2010](#)) and Matplotlib ([Hunter, 2007](#)).

Supplemental materials of this work provide additional information about the characterization of earthquakes occurring in Sardinia and the plot with the model used for the seismic amplitude ratio simulations.

## Acknowledgments

This study has been conducted within the framework agreement between Istituto Nazionale di Fisica Nucleare (INFN) and Istituto Nazionale di Geofisica e Vulcanologia (INGV). The authors would also like to acknowledge INFN that funded this project thanks to the Protocollo di Intesa tra Ministero dell'Istruzione, dell'Università e della Ricerca, la Regione Autonoma della Sardegna, l'Istituto Nazionale di Fisica Nucleare e l'Università degli Studi di Sassari finalizzato a sostenere la candidatura italiana a ospitare l'infrastruttura Einstein Telescope in Sardegna e al potenziamento di Virgo, and the University of Sassari that funded this project thanks to the Accordo di Programma tra la Regione Autonoma della Sardegna, l'Università degli Studi di Sassari, l'Istituto Nazionale di Fisica Nucleare, l'Istituto Nazionale di Geofisica e Vulcanologia, l'Università degli studi di Cagliari e l'IGEA S.p.a. finalizzato alla realizzazione nella Regione Autonoma della Sardegna di una infrastruttura a basso rumore sismico e antropico dedicata alla ricerca di base nell'ambito della rivelazione di onde gravitazionali, fisica della gravitazione, geofisica e sue applicazioni (progetto SARDINIA-GRAVITY [SAR-GRAV]). Intervento finanziato con risorse Fondo per lo Sviluppo e la Coesione (FSC) 2014–2020–Patto per lo sviluppo della Regione Sardegna. The authors also acknowledge the Parco Geominerario Storico e Ambientale della Sardegna for its financial support. The authors' grateful acknowledgment also goes to the contribution of the European Cooperation in Science and Technology (COST) Action CA17137 that supported this work by an Short Term Scientific Mission (STSM) Grant and the contribution of the Fondi di Ateneo 2017 of Sapienza—University of Rome. The authors also thank L. Loddo and M. Capello for their support during fieldwork in Sos Enattos and S. Koley of Nationaal instituut voor subatomaire fysica (Nikhef), for discussions and remarks.

## References

- Amann, F., F. Bonsignorio, T. Bulik, H. J. Bulten, S. Cuccuru, A. Dassargues, R. DeSalvo, E. Fenyvesi, F. Fidecaro, I. Fiori, *et al.* (2020). Site-selection criteria for the Einstein Telescope, *Rev. Sci. Instrum.* **91**, 094504.
- Ardhuin, F., L. Gualtieri, and E. Stutzmann (2019). Physics of ambient noise generation by ocean waves, in *Seismic Ambient Noise*, N. Nakata, L. Gualtieri, and A. Fichtner (Editors), Cambridge University Press, 69–108, ISBN: 9781108417082.
- Ardhuin, F., E. Stutzmann, M. Schimmel, and A. Mangeney (2011). Ocean wave sources of seismic noise, *J. Geophys. Res.* **116**, no. C09004, doi: [10.1029/2011JC006952](https://doi.org/10.1029/2011JC006952).
- Atakan, K., A. M. Duval, N. Theoudilidis, B. Guillier, J. L. Chatelain, P. Y. Bard, and The SESAME Team (2004). The H/V spectra ratio technique: Experimental conditions, data processing and empirical reliability assessment, *13th World Conf. on Earthquake Engineering*, Vancouver, British Columbia, Canada, 1–6 August 2004, Paper Number 2268.
- Beker, M., J. F. J. van den Brand, E. Hennes, and D. S. Rabeling (2011). Newtonian noise and ambient ground motion for gravitational wave detectors, *Proc. of the 9th Edoardo Amaldi Meeting and*



- the 2011 Numerical Relativity and Data Analysis Meeting, *J. Phys. Conf.*, Vol. 363, 012004.
- Beyreuther, M., R. Barsch, L. Krischer, T. Megies, Y. Behr, and J. Wassermann (2010). ObsPy: A Python toolbox for seismology, *Seismol. Res. Lett.* **81**, no. 3, 530–533.
- Boschi, E., D. Giardini, A. Morelli, G. Romeo, and Q. Taccetti (1991). MedNet: The very broad-band seismic network for the Mediterranean, *Il Nuovo Cimento* **14**, 1–21.
- Cahn, R., and G. Goldhaber (2009). *The Experimental Foundations of Particle Physics*, Cambridge University Press, ISBN: 978-0-511-59551-6.
- Carmignani, L., G. Cornamusini, P. Conti, and M. Meccheri (2004). The internal Northern Apennines, the Northern Tyrrhenian Sea and the Sardinia-Corsica Block, in *The Geology of Italy*, U. Crescenti, S. D'Offizi, S. Merlino, and L. Sacchi (Editors), 59–67.
- Casey, R., M. E. Templeton, G. Sharer, L. Keyson, B. R. Weertman, and T. Ahern (2018). Assuring the quality of IRIS data with MUSTANG, *Seismol. Res. Lett.* **89**, no. 2A, 630–639.
- Chevrot, S., M. Sylvander, S. Benahmed, C. Ponsolles, J. M. Lèfevre, and D. Paradis (2007). Source locations of secondary microseisms in western Europe: Evidence for both coastal and pelagic sources, *J. Geophys. Res.* **112**, no. B11, 301–320.
- Effler, A., R. M. S. Schofield, V. V. Frolov, G. Gonzales, K. Kawabe, J. R. Smith, J. Birch, and R. McCarthy (2015). Environmental influences on the LIGO gravitational wave detectors during the 6th science run, *Class. Quant. Grav.* **32**, no. 3, 035017.
- Einstein Telescope (ET) Science Team (2010). The Einstein Telescope: A third-generation gravitational wave observatory, *Class. Quant. Grav.* **27**, no. 19, 194002.
- Einstein Telescope (ET) Science Team (2011). Einstein gravitational wave telescope conceptual design study, *ET-0106C-10*, available at <http://et-gw.eu/etdsdocument> (last accessed May 2020).
- Eurostat (2019). *Eurostat Regional Yearbook*, Publications Office of the European Union, ISBN: 978-92-76-03504-6.
- Evans, M., and M. Zanolin (2017). Detecting gravitational waves from supernovae with Advanced LIGO, in *Handbook of Supernovae*, A. Alsabti and P. Murdin (Editors), Springer, ISBN: 9783319218458.
- Faccenna, C., T. W. Becker, L. Auer, A. Billi, L. Boschi, J. P. Brun, F. A. Capitanio, F. Funicello, F. Horvath, L. Jolivet, et al. (2014). Mantle dynamics in the Mediterranean, *Rev. Geophys.* **52**, 282–332.
- Güralp (2020). *3ESPCDE Seismometer User Guide*, Guralp Systems Limited, Reading United Kingdom, available at <https://www.guralp.com/documents/DAS-C3E-0002.pdf> (last accessed May 2020).
- Harms, J. (2019). Terrestrial gravity fluctuations, *Living Rev. Relativ.* **22**, 6.
- Herrmann, R. B. (2013). Computer programs in seismology: An evolving tool for instruction and research, *Seismol. Res. Lett.* **84**, no. 6, 1081–1088.
- Hild, S., S. Chelkowski, J. Franc, N. Morgado, R. Flaminio, and R. Desalvo (2009). A Xylophone configuration for a third generation gravitational wave detector, *Class. Quant. Grav.* **27**, no. 1, 015003.
- Hillers, G., N. Graham, M. Campillo, S. Kedar, M. Landès, and N. Shapiro (2012). Global oceanic microseism sources as seen by seismic arrays and predicted by wave action models, *Geochem. Geophys. Geosys* **13**, no. 1, doi: [10.1029/2011GC003875](https://doi.org/10.1029/2011GC003875).
- Hunter, J. D. (2007). Matplotlib: A 2D graphics environment, *Comput. Sci. Eng.* **9**, no. 3, 90–95.
- Istituto Nazionale di Geofisica e Vulcanologia (INGV) Seismological Data Centre (2006). Rete Sismica Nazionale (RSN), Istituto Nazionale di Geofisica e Vulcanologia (INGV), Italy, doi: [10.13127/SD/X0FXNH7QFY](https://doi.org/10.13127/SD/X0FXNH7QFY).
- Italian Seismological Instrumental and Parametric Database (ISIDE) Working Group (2007). Italian Seismological Instrumental and Parametric Database (ISIDE), Istituto Nazionale di Geofisica e Vulcanologia (INGV).
- KAGRA Collaboration (2019). KAGRA: 2.5 generation interferometric gravitational wave detector, *Nat. Astron.* **3**, 35–40.
- Konno, K., and T. Ohmachi (1998). Ground-motion characteristics estimated from spectral ratio between horizontal and vertical components of microtremor, *Bull. Seismol. Soc. Am.* **88**, 228–241.
- Korres, G., M. Ravdas, A. Zacharioudaki, A. Chalkiopoulos, D. Denaxa, and R. Lecci (2019). Product user manual for Mediterranean sea waves analysis and forecasting product, available at <http://resources.marine.copernicus.eu/documents/PUM/CMEMS-MED-PUM-006-017.pdf> (last accessed May 2020).
- Levshin, A., V. F. Pisarenko, and G. A. Pogebrinski (1972). On a frequency-time analysis of oscillations, *Ann. Geophys.* **28**, 211–218.
- LIGO Scientific Collaboration (2015). Advanced LIGO, *Class. Quant. Grav.* **32**, no. 7, 074001.
- LIGO Scientific Collaboration and Virgo Collaboration (2019a). All-sky search for continuous gravitational waves from isolated neutron stars using advanced LIGO O2 data, *Phys. Rev. D* **100**, 024004.
- LIGO Scientific Collaboration and Virgo Collaboration (2019b). GWTC-1: A gravitational-wave transient catalog of compact binary mergers observed by LIGO and Virgo during the first and second observing runs, *Phys. Rev. X* **9**, 031040.
- Lomax, A., A. Michelini, and A. Curtis (2009). Earthquake location, direct, global-search methods in complexity, in *Encyclopedia of Complexity and System Science*, Part 5, Springer, 2449–2473.
- Longuet-Higgins, M. S. (1950). A theory of the origin of microseisms, *Phil. Trans. Roy. Soc. Lond. A* **243**, 1–35.
- Lunedei, E., and P. Malischewsky (2015). A review and some new issues on the theory of the H/V technique for ambient vibrations, in *Perspectives on European Earthquake Engineering and Seismology*, A. Ansal (Editor), Geotechnical, Geological and Earthquake Engineering, 39, Springer, Cham, Switzerland.
- Magrini, F., G. Diaferia, I. Fadel, F. Cammarano, M. van der Meijde, and L. Boschi (2020). 3-D shear wave velocity model of the lithosphere below the Sardinia-Corsica continental block based on Rayleigh-wave phase velocities, *Geophys. J. Int.* **220**, 2119–2130.
- McNamara, D. E., and R. P. Buland (2004). Ambient noise levels in the continental United States, *Bull. Seismol. Soc. Am.* **94**, no. 4, 1517–1527.
- Nakamura, Y. (1989). A method for dynamic characteristics estimation of subsurface using microtremor on the ground surface, *Q. Rep. Railway Tech. Res. Inst.* **30**, no. 1, 25–33.
- Nakamura, Y. (2008). On the H/V spectrum, *Proc. of the 14th World Conf. on Earthquake Engineering*, Beijing, China, 12–17 October 2008.
- Nanometrics (2005). *Trillium 240 Seismometer User Guide*, Nanometrics Inc., Kanata, Ontario, Canada.
- Naticchioni, L. (2018). SARGRAV: The Sardinia Underground Laboratory, a first module for the Einstein Telescope



- infrastructure, *Proc. of the 2018 Gravitational Wave Science & Technology Symposium*, Padova, Italy, 1–2 March 2018.
- Naticchioni, L., V. Boschi, E. Calloni, M. Capello, A. Cardini, M. Carpinelli, S. Cuccuru, M. D'Ambrosio, R. De Rosa, M. Di Giovanni, *et al.* (2020). Characterization of the Sos Enattos site for the Einstein Telescope, *Proc. of the 16th International Conf. on Topics in Astroparticle and Underground Physics, J. Phys. Conf.*, Vol. 1468, 012242.
- Naticchioni, L., M. Perciballi, F. Ricci, E. Coccia, V. Malvezzi, F. Acernese, F. Barone, G. Giordano, R. Romano, M. Punturo, *et al.* (2014). Microseismic studies of an underground site for a new interferometric gravitational wave detector, *Class. Quant. Grav.* **31**, no. 10, 105016.
- Parolai, S., P. Bormann, and C. Milkereit (2002). New relationships between Vs, thickness of sediments, and resonance frequency calculated by the H/V ratio of seismic noise for the Cologne area (Germany), *Bull. Seismol. Soc. Am.* **92**, no. 6, 2521–2527.
- Peterson, J. (1993). *Observations and modeling of seismic background noise*, U.S. Geol. Surv. Open-File Rept. 93322.
- Piccinini, D., C. Giunchi, M. Olivieri, F. Frattini, M. Di Giovanni, G. Prodi, and C. Chiarabba (2020). COVID-19 lockdown and its latency in Northern Italy: Seismic evidence and socio-economic interpretation, *Sci. Rep.* **10**, 16487.
- Poli, P., J. Boaga, I. Molinari, V. Cascone, and L. Boschi (2020). The 2020 coronavirus lockdown and seismic monitoring of anthropic activities in Northern Italy, *Sci. Rep.* **10**, 9404.
- Rovida, A., M. Locati, R. Camassi, B. Lolli, and P. Gasperini (2019). *Catalogo Parametrico dei Terremoti Italiani (CPTI15), versione 2.0*, Istituto Nazionale di Geofisica e Vulcanologia (INGV).
- Saccorotti, G., D. Piccinini, L. Cauchie, and I. Fiori (2011). Seismic noise by wind farms: A case study from the VIRGO gravitational wave observatory, Italy, *Class. Quant. Grav.* **101**, no. 2, 568–578.
- Saulson, P. R. (1984). Terrestrial gravitational noise on a gravitational wave antenna, *Phys. Rev. D* **30**, no. 4, 732–736.
- Schroeder, D. J. (2000). *Astronomical Optics*, Academic Press, ISBN: 978-0-12-629810-6.
- Stucchi, M., C. Meletti, V. Montaldo, A. Akinci, E. Faccioli, P. Gasperini, L. Malagnini, and G. Valensise (2004). Pericolosità sismica di riferimento per il territorio nazionale MPS04 [Data set], Istituto Nazionale di Geofisica e Vulcanologia (INGV) (in Italian).
- Stucchi, M., C. Meletti, V. Montaldo, H. Crowley, G. M. Calvi, and E. Boschi (2011). Seismic hazard assessment (2003–2009) for the Italian Building code, *Bull. Seismol. Soc. Am.* **101**, no. 4, 1885–1911.
- Virgo Collaboration (2004). Properties of seismic noise at the Virgo site, *Class. Quant. Grav.* **21**, no. 5, S433.
- Virgo Collaboration (2006). Environmental noise studies in Virgo, *J. Phys. Conf.* **32**, no. 1, 80.
- Virgo Collaboration (2010). Noise from scattered light in Virgo's second science run data, *Class. Quant. Grav.* **27**, no. 19, 194011.
- Virgo Collaboration (2011). The seismic superattenuators of the Virgo gravitational waves interferometer, *J. Low Freq. Noise Vib. Active Contr.* **30**, 63–79.
- Virgo Collaboration (2015). Advanced Virgo: A second-generation interferometric gravitational wave detector, *Bull. Seismol. Soc. Am.* **32**, no. 2, 024001.
- Wathelet, M., J.-L. Chatelain, C. Cornou, G. Di Giulio, B. Guillier, M. Ohrnberger, and A. Savvaidis (2020). Geopsy: A user-friendly open-Source tool set for ambient vibration processing, *Seismol. Res. Lett.* **91**, no. 3, 1878–1889.
- Woessner, J., L. Danciu, D. Giardini, and the SHARE consortium (2015). The 2013 European Seismic Hazard Model: Key components and results, *Bull. Earthq. Eng.* **13**, 3553–3596.

---

Manuscript received 12 May 2020

Published online 4 November 2020